0254-6124/2026/46(5)-0001-12 *Chin. J. Space Sci.* 空间科学学报

ZHANG Ning, YUE Xin'an, ZHOU Xu, CAI Yihui, WANG Junyi, WANG Yonghui, ZHU Yajun, DING Feng, NING Baiqi. Derivation and Evaluation of Nighttime Zonal Wind in the Thermosphere Based on SYISR Observations. *Chinese Journal of Space Science*, 2026, **46**(5): 1–12. CSTR:32142.14.cjss.2025–0199. DOI:10.11728/cjss2026.05.2025–0199

Derivation and Evaluation of Nighttime Zonal Wind in the Thermosphere Based on SYISR Observations*

ZHANG Ning[1] YUE Xin'an[1,3] ZHOU Xu[1] CAI Yihui[1]
WANG Junyi[1] WANG Yonghui[1,3] ZHU Yajun[2,3]
DING Feng[1,3] NING Baiqi[1]

1(*Key Laboratory of Planetary Science and Frontier Technology/Beijing National Observatory of Space Environment, Institute of Geology and Geophysics, Chinese Academy of Sciences, Beijing* 100029)

2(*State Key Laboratory of Space Weather and Solar Activity, National Space Science Center, Chinese Academy of Sciences, Beijing* 100190)

3(*College of Earth and Planetary Sciences, University of Chinese Academy of Sciences, Beijing* 100049)

Abstract In our previous studies, using experimental data from Sanya (18.3°N, 109.6°E) Incoherent Scatter Radar (SYISR), we have obtained the line-of-sight ion velocity in multiple directions, subsequently calculated three-dimensional vector velocity through least square fitting, and finally derived electric fields from 200 km to 500 km based on the ion momentum equation. In this study, we further derived nighttime zonal wind from 200 km to 500 km based on the F region dynamo theory. To verify the reliability, we first analyzed the variations and errors of the nighttime zonal wind at different time scales. Then, we used an empirical model (HWM) and a theoretical model (NCAR-TIEGCM) for comparative analysis. Model results and observation results had a relatively good consistency. The maximum nighttime zonal wind velocity from the SYISR (HWM, TIEGCM) is 115.6 $m \cdot s^{-1}$ (144.3 $m \cdot s^{-1}$, 92.1 $m \cdot s^{-1}$) for the monthly average value. We further compared the nighttime zonal wind from the SYSISR with that from a co-located FPI. They showed a positive correlation with a coefficient of ～0.68 for the zonal wind values, demonstrating a strong consistency between the two independent observation techniques.

Key words Sanya Incoherent Scatter Radar (SYISR), Zonal wind, Momentum equation, F region dynamo theory

Classified index

0 Introduction

Neutral wind transports energy and momentum in the global ionosphere-thermosphere system. Neutral wind carrying charged particles cuts the magnetic field lines to generate an electric field. Plasma motion and neutral winds are tightly coupled with each other. Neutral wind plays an important role in the evolution of large scale (*e.g.*, equatorial ionization anomaly) and small scale (*e.g.,* irregularity) structures in the low-latitude iono-

* Supported by the B-type Strategic Priority Program of the Chinese Academy of Sciences (XDB0780000), the National Natural Science Foundation of China (42504162, 42425403, 42574219), and the Project of Stable Support for Youth Team in Basic Research Field, Chinese Academy of Sciences (YSBR-018)

Received November 25, 2025. Revised February 11, 2026

©The Author(s) 2026. This is an open access article under the CC-BY 4.0 License (https://creativecommons.org/licenses/by/4.0/)

sphere[1–4]. Detecting the variability of neutral winds in the thermosphere is highly important but challenging[5–11].

Fabry-Parrot Interferometers (FPIs) can also measure winds at night, but the observations are generally discontinuous due to light pollution and cloudy weather[12–14]. Spaceborne satellites with onboard optical instruments, such as TIMED/TIDI, and ICON/MIGHTI, detect neutral winds using limb observations and can measure global wind variability on a climatological time scale[15–18]. The disadvantage of satellite measurements is that they are usually limited in local-time coverage at a particular location, so it is difficult to analyze short-term variability of winds[19,20]. Lindzen[21] took the observed diurnal component of the pressure given experimentally by the model and obtained the simplest form of the resulting zonal wind. He found that zonal wind could reach about 300 $m \cdot s^{-1}$ even with a low estimate of the pressure term.

Based on Line-of-Sight (LOS) ion velocity information, neutral winds can also be derived from Incoherent Scatter Radars (ISRs) data, *e.g.* Arecibo ISR data[22–25], EISCAT ISR data[26,27], PFISR data[28,29], and Sanya Incoherent Scatter Radar (SYISR) data[30]. Pointing Arecibo ISR toward geomagnetic north (353°) and geomagnetic south (173°) respectively (by rotating the antenna) for 10 minutes, Behnke[22] *et al.* obtained the velocity along the geomagnetic field line and the velocity perpendicular to the geomagnetic field line in the geomagnetic meridian plane. Then the meridional neutral wind in the F region is calculated. Nygren[25] *et al*. used EISCAT ISR data to calculate the electric field and neutral wind. They first calculated two electric fields in the F region according to the vector velocity perpendicular to the magnetic field line, and then calculated the neutral wind in the E region by using the obtained electric fields and the vector velocity. Heinselman and Nicolls[27] used PFISR multi-beam data to calculate vector velocity, electric field in the F region and neutral wind in the E region. The overdetermined problem is solved using the Bayes least squares method, through which the three-dimensional vector velocity is derived from multiple LOS velocities, and the electric field and neutral wind in the E region are obtained. Using SYISR data, we calculated three-dimensional ion velocities and subsequently derived meridional neutral winds and vector electric fields from 150 km to 500 km based on long-pulse observations[1]. The SYISR was further expanded to 8320 antennas with a peak power greater than 4 MW[31]. And then, we used the expanded SYISR to derive neutral winds from 100 km to 150 km at low latitudes based on alternating code pulse observations[2]. However, the above-mentioned ISRs mainly measure the meridional wind in the F region and the neutral wind in the E region, and none of them have been employed to study the zonal wind in the F region.

Using the EISCAT radar data, Bates and Roberts[32] developed a technique to calculate the heat conduction velocity by calculating the upper and lower limits of the ion temperature and the neutral temperature, which is approximately equal to the local Joule heating rate. The calculated local Joule heating rate (dependent on the vector ion-neutral velocity difference) was used to derive the zonal wind at the peak height of the F layer. Roble *et al*.[33] determined the diurnal variation of the neutral thermospheric wind by the diurnal variation of the electron and ion temperatures, electron density and vertical plasma drift from Millstone Hill ISR measurements. They calculated the horizontal neutral wind component along the magnetic declination and the longitudinal derivative of the neutral exospheric temperature. The atmospheric response to various forcing functions is determined using a three-dimensional dynamic model of the neutral thermosphere, with ion drag specified by the electron density measurements. The harmonic components of the pressure force, expressed in terms of latitudinal and longitudinal variations in exospheric temperature, are used to determine the horizontal neutral wind component along the magnetic declination direction based on the model's response coefficients. Appropriate latitudinal and longitudinal pressure gradients are then constructed. The pressure gradients are then used to calculate the diurnal winds for two geomagnetically quiet days over Millstone Hill during the equinox. To our knowledge, the derivation of the zonal wind in the F region has always been a challenge for ISR.

In this study, using ionospheric measurements from the SYISR, we aim to derive nighttime zonal wind from 200 km to 500 km based on the F region dynamo theory. The observational experiment transmitted long pulses of

480μs. The remainder of the paper is organized as follows. In Section 1, we describe in detail the SYISR experiment. Section 2 describes the data analysis, including the ion vector velocity and nighttime zonal wind calculation. Section 3 compares the SYISR, HWM, NCAR-TIEGCM and FPI data. We discuss and summarize the paper in Section 4.

1 Experiment Setup

A long pulse of 480 μs was used to conduct SYISR observation experiments from November 2023 to October 2024, corresponding to a range resolution of 72 km. The pulse repetition period is 16000 μs, which implies a ～3% duty cycle. We used 11 SYISR beams along and perpendicular to the geomagnetic meridian plane, as shown in Figure 1, which is referred to as a cross-type setup. In the geomagnetic meridian plane, the elevation angles were 45°, 60°, 75°, 90°, 75°, 60°, and 45° from south to north. In the plane perpendicular to the geomagnetic meridian plane, the elevation angles were 60°, 75°, 90°, 75°, and 60° from east to west[34]. According to the principle of incoherent scatter detection, the electron density, ion temperature, electron temperature and LOS ion velocity can be obtained by fitting the measured power spectrum with the theoretical spectrum[35]. Taking the data from 4 November 2023, as an example, we show the LOS ion velocity in Figure 1. Here, the LOS direction is defined as positive when approaching the SYISR. As each beam integrates for 30 seconds, the temporal resolution of the data is 5.5 minutes.

Figure 1 shows that there are valid LOS ion velocity values for all 11 beams. The hexagon in the figure represents the effective scanning range, the different colors in the hexagon represent different gain values, and the black dots represent the beam directions marked from 1 to 11. Note that the no - data point in each subplot indicates that the least square fitting in the data inversion is unsuccessful. The number on each subplot is the corresponding beam number and azimuth/elevation angles. The Sanya Local Time (LT) equals UT plus 7.3 h. In Figure1(h), there are some unsuccessful fitting

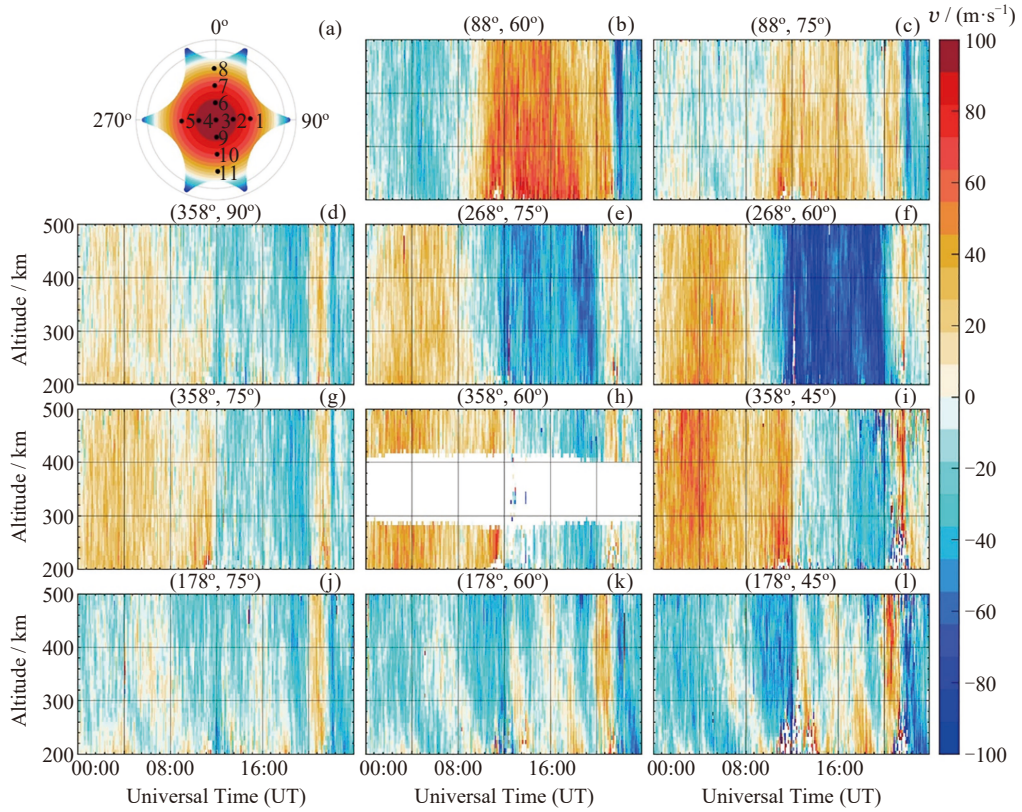


Fig. 1 (a) Beam diagram and LOS velocity for the SYISR experiment used in this study. (b)～(l) Daily universal time - height variations of LOS velocity for 11 beams experiments made on 4 November 2023

points near 300 km, mainly because when the elevation angle is 60° and the azimuth angle is 358°, the radar beam near 300 km is perpendicular to the magnetic field line, which makes the current retrieval algorithm invalid. Figure 1(d) corresponds to the LOS ion velocity in the zenith direction. After 20:00 UT (03:00 LT), a distinct pre-dawn reversal phenomenon can be observed. The LOS ion velocity in the zenith direction is upward during the day and downward during the night. As shown in Figure 1, the LOS ion velocities in different directions are not the same. Figures 1(b) (f) show symmetrical beams with the same elevation angles in the plane perpendicular to the geomagnetic meridian plane. The LOS ion velocities of symmetrical beams are nearly opposite and larger than other beams. The smaller the elevation angle of the beam is, the greater the LOS ion velocities will be.

2 Data Analysis

2.1 Ion Vector Velocity

The ion vector velocity is calculated from the LOS ion velocity. The ion vector velocity and error can be obtained as follows[1]:

$$\boldsymbol{v}_{\mathrm{i}} = \sum\nolimits_{\boldsymbol{v}} \boldsymbol{A}^{\mathrm{T}} \left(\boldsymbol{A} \sum\nolimits_{\boldsymbol{v}} \boldsymbol{A}^{\mathrm{T}} + \sum\nolimits_{\boldsymbol{e}} \right)^{-1} v_{\mathrm{LOS}}, \tag{1}$$

$$\sum\nolimits_{\hat{\boldsymbol{v}}} = \sum\nolimits_{\boldsymbol{v}} - \sum\nolimits_{\boldsymbol{v}} \boldsymbol{A}^{\mathrm{T}} \left(\boldsymbol{A} \sum\nolimits_{\boldsymbol{v}} \boldsymbol{A}^{\mathrm{T}} + \sum\nolimits_{\boldsymbol{e}} \right)^{-1} \boldsymbol{A} \sum\nolimits_{\boldsymbol{v}}. \tag{2}$$

Here, v_{LOS} is the LOS ion velocity. $\boldsymbol{v}_{\mathrm{i}}$ is the ion vector velocity, which is a Gaussian random variable with zero mean, and its covariance is $\sum_{\hat{v}}$. Moreover, $\sum_{v}$ is set as [10000, 0, 0; 0, 10000, 0; 0, 0, 10000], and the units are $\mathrm{m^2 \cdot s^{-2}}$[36]. $\boldsymbol{A}$ is the transformation vector. The measurement error is also regarded as the Gaussian random variable of the zero mean, with a covariance $\sum_{e}$.

The derived ion vector velocities and errors corresponding to the LOS ion velocity of Figure 1 are shown in Figure 2 in the geographic coordinates. Figures 2(a)～(c) show the ion velocity in the eastward, northward and vertical directions. During the day, the ion velocity is mostly westward (northward, upward), and the maximum ion velocity can reach 95.5 $\mathrm{m \cdot s^{-1}}$ (77.6 $\mathrm{m \cdot s^{-1}}$, 16.8 $\mathrm{m \cdot s^{-1}}$). During the night, the ion velocity is mostly eastward (southward, downward), and the maximum ion velocity can reach 153.5 $\mathrm{m \cdot s^{-1}}$ (48.6 $\mathrm{m \cdot s^{-1}}$, 28.8 $\mathrm{m \cdot s^{-1}}$). Figures 2(d)～(f) show the ion velocity errors in the eastward, northward and vertical directions. These figures indicate that the vertical ion velocity error is the smallest, followed by the northward ion velocity error, and the eastward ion velocity error is the largest. The maximum vertical, northward and eastward ion velocity errors are 0.61 $\mathrm{m \cdot s^{-1}}$, 2.48 $\mathrm{m \cdot s^{-1}}$ and 5.76 $\mathrm{m \cdot s^{-1}}$ from 200 km to 500 km during the day, respectively. The maximum vertical, northward and eastward ion velocity errors are 0.73 $\mathrm{m \cdot s^{-1}}$, 5.52 $\mathrm{m \cdot s^{-1}}$ and 6.06 $\mathrm{m \cdot s^{-1}}$ from 200 km to 500 km during the night, respectively. The third and fourth rows in Figure 2 are the same as the first and second rows but in the geomagnetic coordinates. The ion velocity consists of the eastward component perpendicular to the geomagnetic field line (v_{pe}), the northward component perpendicular to the geomagnetic field line (v_{pn}), and the velocity antiparallel to the geomagnetic field line (v_{ap}). The maximum ion velocities are 97.6 $\mathrm{m \cdot s^{-1}}$, 58.3 $\mathrm{m \cdot s^{-1}}$ and 77.1 $\mathrm{m \cdot s^{-1}}$ for v_{pe} v_{pn} and v_{ap} during the day, respectively. Most errors in v_{pe}, v_{pn}, and v_{ap} do not exceed 7.37 $\mathrm{m \cdot s^{-1}}$, 1.38 $\mathrm{m \cdot s^{-1}}$ and 4.8 m/s during the day, respectively. The maximum ion velocities are 157.5 $\mathrm{m \cdot s^{-1}}$, 39.2 $\mathrm{m \cdot s^{-1}}$ and 78.1 $\mathrm{m \cdot s^{-1}}$ for v_{pe}, v_{pn} and v_{ap} during the night, respectively. Most errors in v_{pe}, v_{pn}, and v_{ap} do not exceed 8.09 $\mathrm{m \cdot s^{-1}}$, 2.03 $\mathrm{m \cdot s^{-1}}$ and 5.68 $\mathrm{m \cdot s^{-1}}$ during the night, respectively.

2.2 Night Zonal wind

After we get the ion velocity, we can further derive the electric field in geomagnetic coordinates as follows:

$$E_{\mathrm{pn}} = -v_{\mathrm{pe}} B, \tag{3}$$

$$E_{\mathrm{pe}} = v_{\mathrm{pn}} B. \tag{4}$$

We can further obtain the vertical electric fields in the geographical coordinate system

$$E_{\mathrm{v}} = E_{\mathrm{pn}} \cos I. \tag{5}$$

During the night, an electric field is generated by the movement of electrons or ions driven by the neutral wind in the F region. The zonal wind is generally westward during the day and eastward during night. The eastward wind at night will drive positive charges to accumulate at the upper boundary and negative charges to accumulate at the lower boundary. Therefore, a vertical polarization electric field will be generated, and the polar-

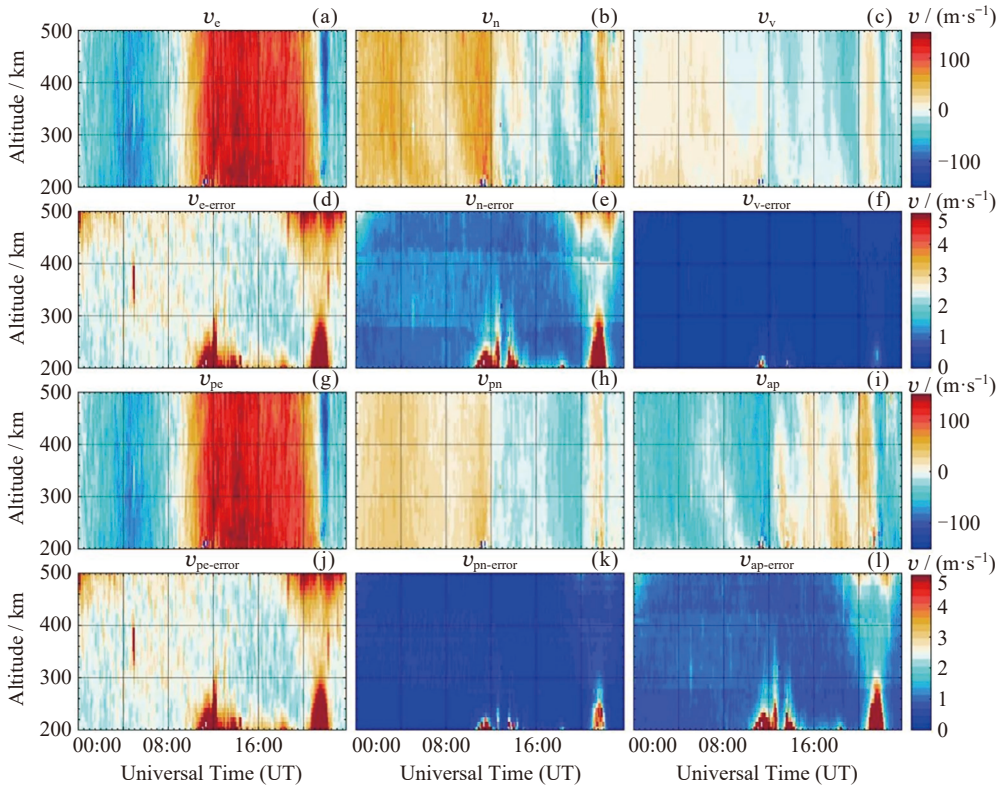


Fig. 2 Universal time and height variations in the vector ion velocity (the first and third rows) and corresponding error (the second and fourth rows) for geographic coordinates (the first and second rows) and geomagnetic coordinates (the third and fourth rows), respectively on 4 November 2023

ization electric field will drive electrons and ions to move under the action of the Lorentz force. Therefore, the vertical electric field E_v in the F region at night detected by the ISR is primarily driven by the zonal wind in the F region[3,7,21,37]. Therefore, we can obtain the zonal wind in the F region during the night by the vertical electric field under the assumption that the dynamo effect of meridional wind is negligible in comparison with that of zonal wind[38,39].

$$u_e = \frac{E_v}{B \cos I \cos D}. \tag{6}$$

Figure 3 shows the calculated nighttime zonal winds on November 4, 2023, and their corresponding errors. Figure 3(a) shows that the zonal wind is eastward, and the maximum velocity of 183 m·s^{-1} occurs at 14:00 UT at approximately 200 km. Figure 5(b) shows that the maximum zonal wind error is 17 m·s^{-1} at 200 km around 11:00 UT, mainly due to relatively low electric density. Most zonal wind errors do not exceed 5 m·s^{-1} above 250 km. The winds are eastward and quite strong (about 150 m·s^{-1}) in the post-sunset period, decaying to less than 50 m·s^{-1} after midnight. Airglow observations in the Peruvian sector are in good agreement with these variations[40]. Our results show the same variations: the zonal wind gradually decreases after midnight.

Furthermore, the height variations in the monthly mean (November 2023) and standard deviation of the nighttime zonal wind are plotted in Figure 4 for different local times. Figures 4(a)～(j) show that the standard deviation of the zonal wind after 16:00 UT is larger than that before 16:00 UT. After midnight, the electron density decreases and the radar signal-to-noise ratio drops. Consequently, the quality of the corresponding data decreases, leading to an increase in the standard deviation of the data. The mean values (standard deviations) are 106.23 m·s^{-1} (21.29 m·s^{-1}) for the zonal winds at 15:00 UT at 300 km. The mean values (standard deviations) are 85.05 m·s^{-1} (31.54 m·s^{-1}) for the zonal winds at 17:00 UT at 300 km. As can be seen from Figure 4, the height gradient for zonal wind throughout the night is small.

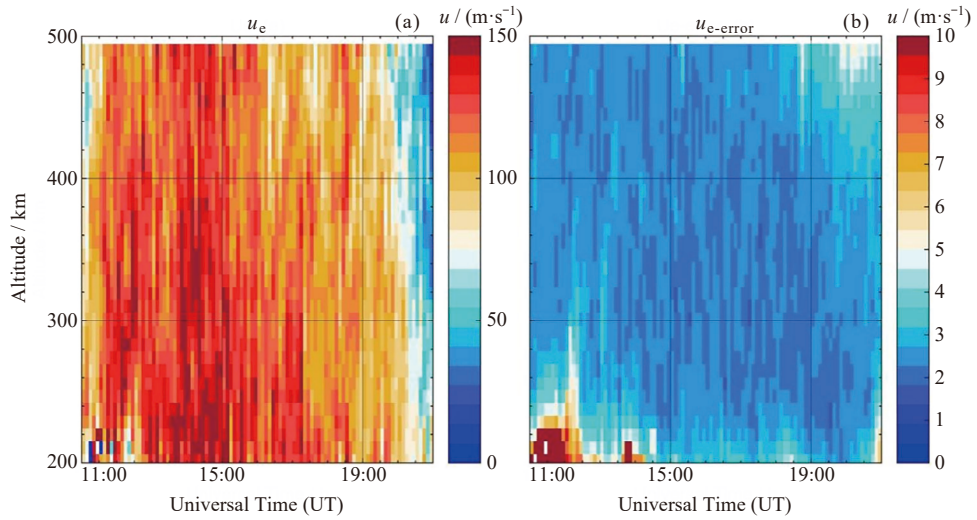


Fig. 3 The calculated zonal winds and corresponding errors in geographic coordinates on 4 November 2023. Note that the colormap range is different between the velocity and its error

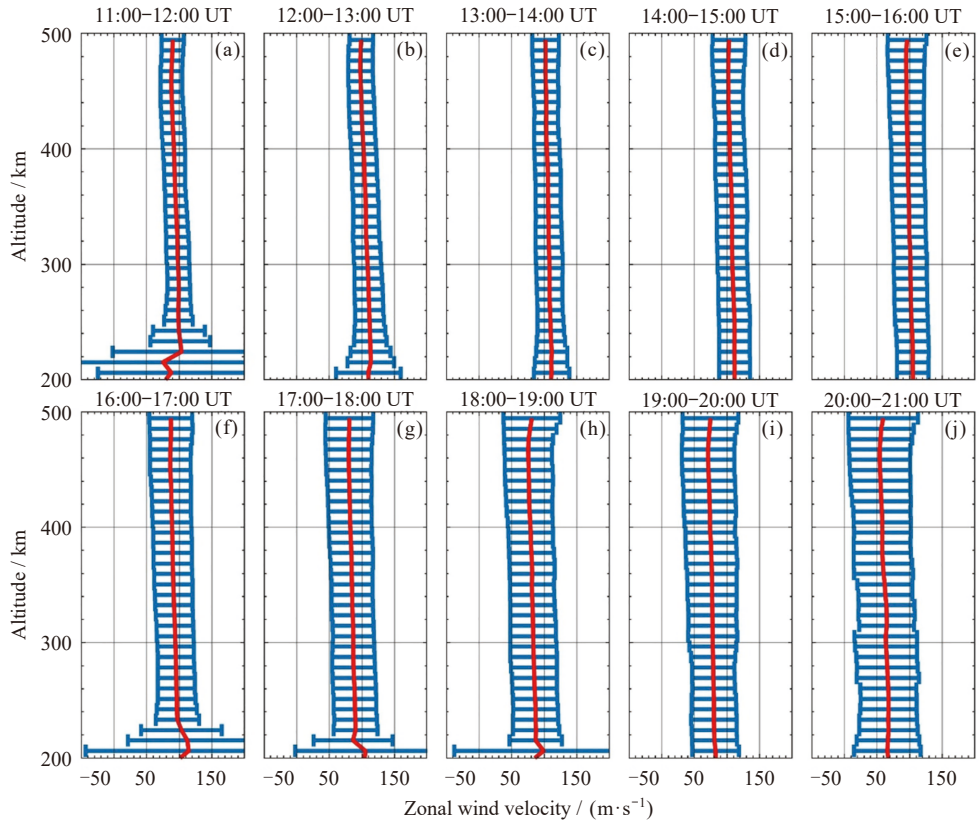


Fig. 4 Monthly mean and standard deviation of the zonal wind varying with height from 200 to 500 km for several selected universal times

3 Data comparison and Discussion

3.1 Comparison among the SYISR, HWM and TIEGCM

To validate the SYISR derived nighttime zonal wind, we compared the average zonal winds observed by the SYISR in geographical coordinates with those from the Horizontal Wind Model version 14 (HWM14)[41,42] and TIEGCM version 2.1[43,44] from November 1, 2023, to November 30, 2023, as shown in Figure 5. The

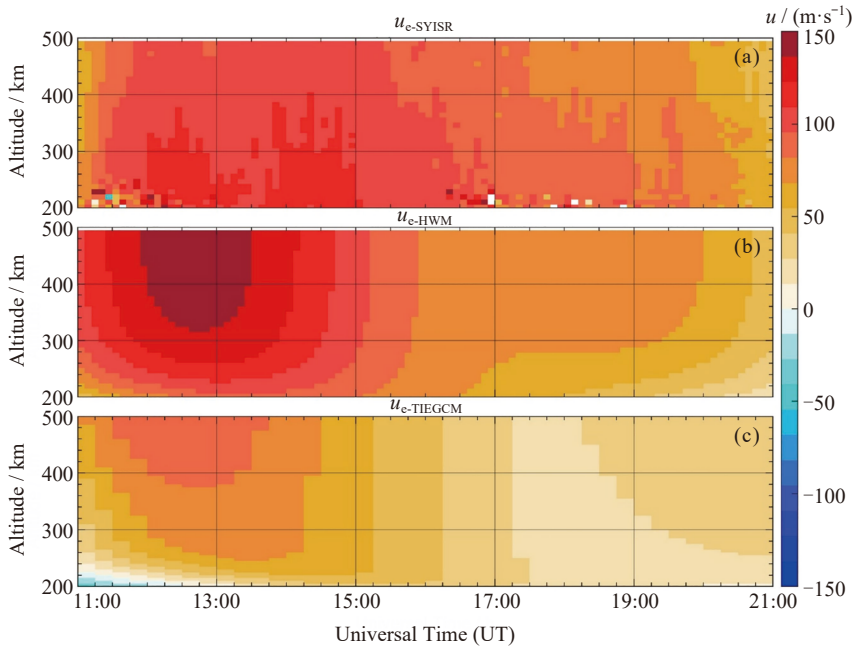


Fig. 5 Universal time and height variations in the monthly average of the zonal wind for the SYISR (a), HWM (b), and TIEGCM (c)

HWM14 was driven by realistic solar activity and geomagnetic indices. We ran the TIEGCM for 30 days, which was driven by realistic solar activity, geomagnetic and interplanetary indices with the Global Scale Wave Model (GSWM) specifying the lower boundary, and Weimer-05[45] modeled polar electric potential. The TIEGCM was run with a resolution of 2.5° in latitude and longitude, 0.25 scale height in altitude, and 30 s in timestep.

Figure 5 shows the nighttime zonal winds from the SYISR, HWM and TIEGCM. The zonal winds from the three kinds of data are similar but have differences. The three kinds of data sets show eastward neutral winds between 11:00 UT and 21:00 UT, in which the SYISR, HWM and TIEGCM maximum velocities are 115.6 m·s^{-1}, 144.3 m·s^{-1} and 92.1 m·s^{-1} around 13:00 UT, respectively. The velocity from HWM is slightly greater than that from SYISR and TIEGCM. According to Figures 5(b) (c), there are also differences in the zonal winds between those from TIEGCM and HWM. Figures 5(a), (b) and (c) show that the zonal neutral winds from the SYISR and those of the HWM and those of the TIEGCM. The variations of the zonal neutral winds of the SYISR and HWM are similar after midnight, but there are still some differences between the zonal winds of the SYISR and HWM. All three types of winds show their maximum nearly simultaneously at 13:00 UT and then gradually decrease. After 17:00 UT, the zonal wind of TIEGCM drops below 50 m·s^{-1}, while the zonal wind of HWM and SYISR remain above 50 m·s^{-1}.

To further show the day-to-day variability of the three datasets, we plotted the zonal winds during a geomagnetic quiet period of 11-20 November 2023 in Figure 6. Figures 6(a), (b), and (c) correspond to the zonal winds of the three datasets, respectively. For the HWM and TIEGCM, the daily zonal neutral winds are almost the same during this period, but the nighttime zonal winds of HWM results are larger than those of TIEGCM results. On the other hand, the daytime zonal winds of HWM results are smaller than those of TIEGCM results. A likely reason is that the empirical model incorporates observational data, leading to incomplete consistency with the theoretical model. For the wind derived from SYISR data, the daily zonal neutral winds are similar to those during the geomagnetic quiet period, and there is a relatively large zonal neutral wind after 19 November 2023. The maximum eastward velocity occurs on November 21 for the SYISR, with a maximum value of 146.2 m·s^{-1}. Among the nighttime zonal winds from

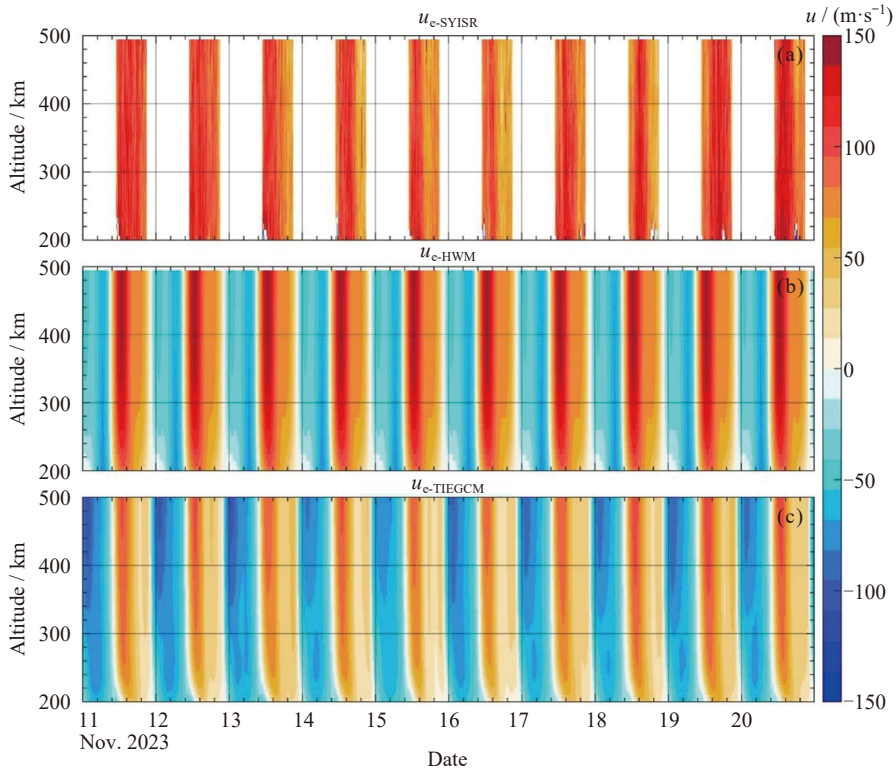


Fig. 6 The variations in the zonal neutral winds of the SYISR (a), HWM (b) and TIEGCM (c) versus date and height from 11-20 November 2023

SYISR, TIEGCM and HWM, the consistency of those from SYISR and HWM is better than that of those from SYISR and TIEGCM. A crucial reason is that HWM has observational data, while TIEGCM is entirely based on theoretical models. There are certain differences between theoretical models and observations. Therefore, the results of SYISR and HWM are more consistent.

3.2 Comparison between the Zonal Wind Results from SYISR and FPI

To further validate our method and results, we also compared with a co-located FPI neutral wind[13,14] from Danzhou (19.5°N, 109.1°E) with SYISR wind data from November 2023 to January 2024 around 250 km. The data of SYISR during the nighttime (13:00—20:00 UT) was compared with the FPI data. Figure 7 shows some example comparison for 6 selected dates. Both the FPI zonal wind data and the SYISR zonal wind data are in good agreement and in the range from -50 m·s^{-1} to 150 m·s^{-1}. The nighttime zonal wind is predominantly eastward, reversing direction only on a few days. These results indicate a good consistency despite the different detection principles between SYISR and FPI.

In order to further carry out statistical analysis of the zonal wind, we compared the data of FPI with the data of SYISR from 1 November 2023 to 19 January 2024, and drew a scatter plot, as shown in the Figure 8. Figure 8 demonstrates that the FPI and SYISR neutral wind measurements are positively correlated, and the correlation coefficient was 0.68. The mean and standard deviation of the difference between two measurements is 23.8 m·s^{-1} and 22.1 m·s^{-1}, respectively. Note that we did not do any smoothing or quality control when making this comparison. On the other hand, we can find the zonal wind of SYISR is slightly larger than FPI, and the main reason is the different detection principles and data processing. These results demonstrate good consistency between the SYISR and FPI zonal wind observations.

4 Discussion and Summary

In this study, we calculated the nighttime zonal winds in the thermosphere using long pulses generated by the SYISR in the low - latitude region of China from 200 to 500 km. To our knowledge, only EISCAT ISR and Mill-

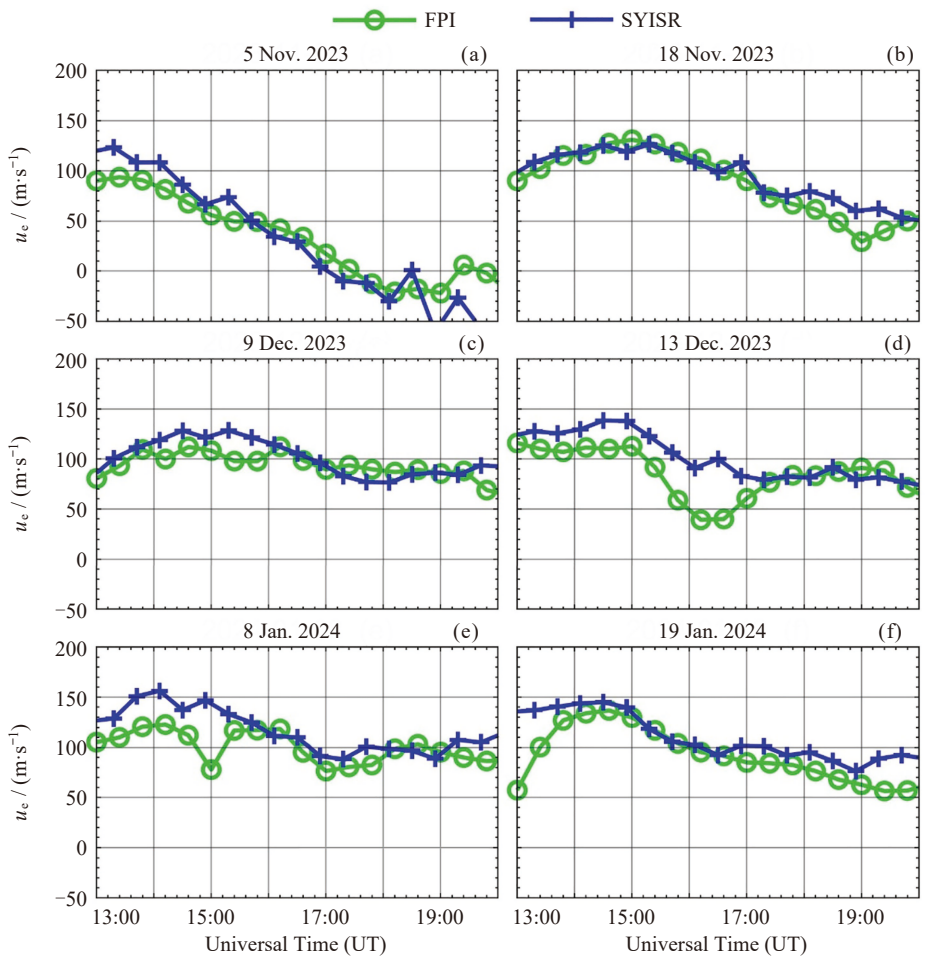


Fig. 7 Comparison of the zonal wind around 250 km altitude observed by FPI and SYISR at different times

stone Hill ISR measurements have been used to conduct research on F region zonal wind. The inversion method used by EISCAT ISR relies on Joule heating, and only suitable for the ISRs in the high-latitude regions. Millstone Hill ISR, located at mid-latitudes, employs a thermospheric dynamic model and calculates F region zonal winds using parameters such as the temperature gradient derived from ISR measurements as we described in the introduction section. SYISR, located at low latitudes, has dynamical processes approximating those around the magnetic equator, and low-latitude F-region dynamics can be used. It is a relatively simple methods and needs minimal assumptions to derive nighttime F-region zonal winds. However, daytime dynamics are dominated by the E-region dynamo at low latitudes, so only nighttime zonal winds in the F region can be obtained based on SYISR observations.

Figure 5 shows that the zonal wind increases after sunset and decreases after midnight. After sunset, the zonal wind exhibits a distinct enhancement peak. One important reason is that solar heating ceases after sunset, creating a strong horizontal temperature gradient between the daytime-heated regions (such as low-latitude areas) and the cooling nighttime regions, which readily translates into intense eastward zonal winds, particularly at thermospheric altitudes. Another reason is that the dynamo process in the F-layer generates a stronger eastward electric field. This enhanced electric field efficiently drives the thermospheric neutral atmosphere to produce stronger eastward winds through the ion-drag effect.

After midnight, the enhanced eastward wind usually weakens and may even reverse to a westward wind. The first reason is that the upper atmosphere undergoes continuous radiative cooling during the night, altering the pressure field—a process that tends to weaken or re-

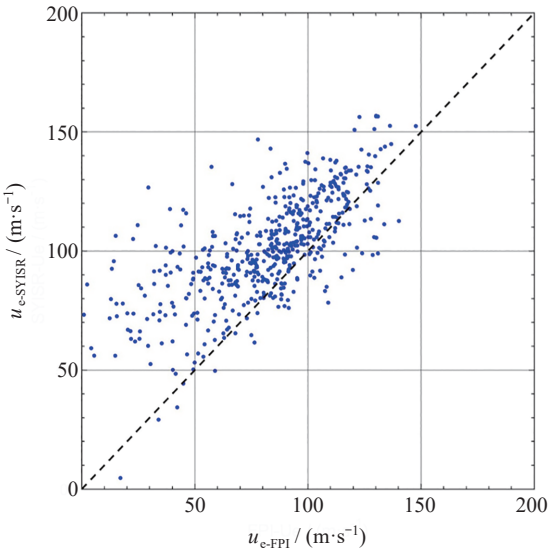


Fig. 8 Comparison of the zonal wind around 250 km altitude between the FPI and SYISR measurements for three months. The black dashed line in the figure represents the diagonal line

verse the eastward zonal wind over the equator. The second reason is that the plasma density decreases significantly at night, greatly reducing the ability of ions to couple with and drag the neutral wind, making it impossible to sustain the strong post-sunset eastward wind. The final reason is that tidal waves propagating upward from the lower atmosphere have significant amplitudes in the thermosphere. Their wind components superimpose on the background wind, which can lead to its weakening or reversal.

After obtaining the nighttime zonal wind in the F region, we further validated the derived nighttime zonal winds. We compared the SYISR zonal winds with the model results from HWM and TIEGCM and the observed results from a co-located FPI. We verified the accuracy of the observed nighttime zonal winds. The main conclusions are as follows.

Firstly, the SYISR, HWM and TIEGCM zonal winds show similar diurnal and day - to - day variations. The maximum neutral wind velocity from the SYISR (HWM, TIEGCM) is 115.6 m·s^{-1} (144.3 m·s^{-1}, 92.1 m·s^{-1}) for the monthly average value.

Secondly, the FPI and SYISR wind at 250 km are consistent. Statistically, they have a relatively high correlation coefficient of 0.68. The differences in the mean and standard deviation between the two measurements for the nighttime zonal winds are respectively 23.8 m·s^{-1} and 22.1 m·s^{-1}.

As we described earlier, for the ground-based observation methods, the detection of zonal winds in the thermosphere is rather challenging. The zonal winds derived through our calculations are of great significance. They can not only be used to analyze the low-latitude dynamic processes, but also have important value for the validation and improvement of global circulation models.

Acknowledgements We acknowledge the use of SYISR data from the Chinese Meridian Project.

Ethical Approval This article does not contain any studies with human participants or animals performed by any of the authors.

Conflict of Interests The authors declare that there is no conflict of interests.

References

[1] ZHANG N, YUE X N, CAI Y H, *et al*. F region neutral wind and electric field measured by SYISR and evaluation[J]. *Journal of Geophysical Research: Space Physics*, 2024, **129**(5): e2024JA032514

[2] ZHANG N, YUE X N, WANG J Y, *et al*. Calculation and evaluation of neutral winds in the lower thermosphere based on SYISR observations[J]. *Journal of Geophysical Research: Space Physics*, 2024, **129**(11): e2024JA032994

[3] FORBES J M, LINDZEN R S. Atmospheric solar tides and their electrodynamics effects—I. the global S_q current system[J]. *Journal of Atmospheric and Terrestrial Physics*, 1976, **38**(9/10): 897-910

[4] HANSON W B, MOFFETT R J. Ionization transport effects in the equatorial F region[J]. *Journal of Geophysical Research*, 1966, **71**(23): 5559-5572

[5] HARPER R M. Tidal winds in the 100- to 200-km region at Arecibo[J]. *Journal of Geophysical Research*, 1977, **82**(22): 3243-3250

[6] MARSH D R. Chemical–dynamical Coupling in the Mesosphere and Lower Thermosphere[M]//ABDU M A, PANCHEVA D. Aeronomy of the Earth's Atmosphere and Ionosphere. Dordrecht: Springer, 2011: 3-17

[7] MATSUSHITA S. Dynamo currents, winds, and electric fields[J]. *Radio Science*, 1969, **4**(9): 771-780

[8] SHENG Z, HE Y, WANG S C, *et al*. Dynamics, chemistry, and modeling studies in the aviation and aerospace transition zone[J]. *The Innovation*, 2025, **6**(8): 101012

[9] XIAO Zuo. Researches on ionospheric physics in recent years in China[J]. *Acta Geophysica Sinica*, 1997, **40**(S1): 21-28 (肖佐. 近年来中国电离层物理研究进展 [J]. 地球物理学报, 1997, **40**(S1): 21-28)

[10] XIAO Zuo, LIU Kaijun, ZHANG Donghe. Some typical records of ionospheric doppler shift and their significance in the study of ionospheric morphology[J]. *Chinese Journal of Space Science*, 2002, **22**(4): 321-329 (肖佐, 刘凯军, 张东和. 典型电离层多普勒记录及其讨论 [J]. 空间科学学报, 2002, **22**(4): 321-329)

[11] XIONG Chao, RANG Xinyi, HUANG Yuyang, *et al*. Latitudinal four-peak structure of the nighttime F region ionosphere: possible contribution of the neutral wind[J]. *Reviews of Geophysics and Planetary Physics*, 2024, **55**(1): 94-108 (熊超, 让心怡, 黄宇阳, 等. 中性风对夜侧电离层纬向四峰结构的影响 (英文)[J]. 地球与行星物理论评 (中英文), 2024, **55**(1): 94-108)

[12] WANG Houmao, WANG Yongmei, WANG Yingjian, *et al*. Wind retrieval and error analysis of ground-based Fabry-Perot interferometer for the middle and upper atmosphere[J]. *Chinese Journal of Space Science*, 2014, **34**(4): 415-425 (王后茂, 王咏梅, 王英鉴, 等. 地基 Fabry-Perot 中高层大气风速反演及误差分析 [J]. 空间科学学报, 2014, **34**(4): 415-425)

[13] WANG T C, ZHU Y J, ZHU G Y, *et al*. Development and experimental validation of a signal-tracking Fabry-Perot interferometer for upper atmospheric wind measurements[J]. *Optics Express*, 2025, **33**(19): 39724-39739

[14] ZHU G Y, ZHU Y J, KAUFMANN M, *et al*. An efficient calibration system of optical interferometer for measuring middle and upper atmospheric wind[J]. *Remote Sensing*, 2023, **15**(7): 1898

[15] EASTES R W, MCCLINTOCK W E, CODRESCU M V, *et al*. Global-scale observations of the limb and disk (Gold): new observing capabilities for the ionosphere-thermosphere[J]. *Geophysical Monograph Series*, 2008, **181**: 319-326

[16] ENGLERT C R, HARLANDER J M, BROWN C M, *et al*. Michelson Interferometer for Global High-resolution Thermospheric Imaging (MIGHTI): instrument design and calibration[J]. *Space Science Reviews*, 2017, **212**(1/2): 553-584

[17] KILLEEN T L, SKINNER W R, JOHNSON R M, *et al*. TIMED Doppler Interferometer (TIDI)[C]//Optical Spectroscopic Techniques and Instrumentation for Atmospheric and Space Research III. Denver: SPIE, 1999: 289-301

[18] LU Maolin, YI Wen, ZENG Jie, *et al*. Two-dimensional wind field observation based on multistatic meteor radars in central and eastern China[J]. *Reviews of Geophysics and Planetary Physics*, 2024, **55**(3): 329-343 (鲁茂林, 易稳, 曾洁, 等. 基于中国中东部多站流星雷达的二维风场观测研究 [J]. 地球与行星物理论评, 2024, **55**(3): 329-343)

[19] ZHOU X, YUE X N, YU Y, *et al*. Day-to-day variability of the MLT DE3 using joint analysis on observations from TIDI-TIMED and a meteor radar meridian chain[J]. *Journal of Geophysical Research: Atmospheres*, 2022, **127**(3): e2021JD035794

[20] ZHOU Xu, YUE Xin'an, CHEN Guiwan, *et al*. MJO modulation on the intraseasonal variability of MLT DE3 tide in winds[J]. *Chinese Journal of Geophysics*, 2023, **66**(12): 4817-4827 (周旭, 乐新安, 陈桂万, 等. MJO 与中间层-低热层风场潮汐 DE3 季节内变化性的关联 [J]. 地球物理学报, 2023, **66**(12): 4817-4827)

[21] LINDZEN R S. Crude estimate for the zonal velocity associated with the diurnal temperature oscillation in the thermosphere[J]. *Journal of Geophysical Research*, 1966, **71**(3): 865-870

[22] APONTE N, NICOLLS M J, GONZÁLEZ S A, *et al*. Instantaneous electric field measurements and derived neutral winds at Arecibo[J]. *Geophysical Research Letters*, 2005, **32**(12): L12107

[23] BEHNKE A, DOUPNIK J R, BANKS P M. A preliminary study of the neutral wind in the Auroral E Region[J]. *Journal of Geophysical Research*, 1973, **78**(34): 8235-8250

[24] HAGFORS T, BEHNKE R A. Measurement of three-dimensional plasma velocities at the Arecibo Observatory[J]. *Radio Science*, 1974, **9**(2): 89-93

[25] HYSELL D L, LARSEN M F, SULZER M P. High time and height resolution neutral wind profile measurements across the mesosphere/lower thermosphere region using the Arecibo incoherent scatter radar[J]. *Journal of Geophysical Research: Space Physics*, 2014, **119**(3): 2345-2358

[26] NYGRÉN T, AIKIO A T, KUULA R, *et al*. Electric fields and neutral winds from monostatic incoherent scatter measurements by means of stochastic inversion[J]. *Journal of Geophysical Research: Space Physics*, 2011, **116**(A5): A05305

[27] STAMM J, VIERINEN J, GUSTAVSSON B. Observing electric field and neutral wind with EISCAT 3D[J]. *Annales Geophysicae*, 2021, **39**(6): 961-974

[28] HEINSELMAN C J, NICOLLS M J. A Bayesian approach to electric field and E-region neutral wind estimation with the Poker Flat Advanced Modular Incoherent Scatter Radar[J]. *Radio Science*, 2008, **43**(5): RS5013

[29] NICOLLS M J, COSGROVE R, BAHCIVAN H. Estimating the vector electric field using monostatic, multibeam incoherent scatter radar measurements[J]. *Radio Science*, 2014, **49**(11): 1124-1139

[30] YUE X N, WAN W X, NING B Q, *et al*. Development of the Sanya incoherent scatter radar and preliminary results[J]. *Journal of Geophysical Research: Space Physics*, 2022, **127**(8): e2022JA030451

[31] YUE X N, NING B Q, JIN L, *et al*. A tristatic phased array radar system in China[J]. *Nature Astronomy*, 2024, **8**(5): 673

[32] BATES H F, ROBERTS T D. A technique for using incoherent scatter to estimate F-region zonal winds during Joule heating[J]. *Journal of Atmospheric and Terrestrial Physics*, 1977, **39**(11/12): 1293-1306

[33] ROBLE R G, EMERY B A, SALAH J E, *et al*. Diurnal variation of the neutral thermospheric winds determined from incoherent scatter radar data[J]. *Journal of Geophysical Research*, 1974, **79**(19): 2868-2876

[34] ZHANG N, LEI J H, YUE X N, *et al*. Determination of the mysterious O^+-O collision frequency factor from the Sanya incoherent scatter radar measurements[J]. *Geophysical Research Letters*, 2025, **52**(16): e2025GL115928

[35] HAO H L, ZHAO B Q, WAN W X, *et al*. Initial ionospheric ion line results and evaluation by Sanya Incoherent Scatter Radar (SYISR)[J]. *Journal of Geophysical Research*: *Space Physics*, 2022, **127**(9): e2022JA030563

[36] JIN Y Y, ZHAO B Q, YUE X N, *et al*. An evaluation of beam configuration to detect the plasma vector velocity: a simulation method based on the SYISR system[J]. *Journal of Geophysical Research*: *Space Physics*, 2023, **128**(6): e2022JA031057

[37] KELLEY M C. The Earth's Ionosphere: Plasma Physics and Electrodynamic[M]. 2nd ed. Cambridge: Academic Press, 2009

[38] BIONDI M A, SAZYKIN S Y, FEJER B G, *et al*. Equatorial and low latitude thermospheric winds: measured quiet time variations with season and solar flux from 1980 to 1990[J]. *Journal of Geophysical Research*: *Space Physics*, 1999, **104**(A8): 17091-17106

[39] CHAPMAN S, LINDZEN R S. Atmospheric Tides: Thermal and Gravitational[M]. New York: Gordon and Breach, 1970

[40] MERIWETHER JR J W, MOODY J W, BIONDI M A, *et al*. Optical interferometric measurements of nighttime equatorial thermospheric winds at Arequipa, Peru[J]. *Journal of Geophysical Research*: *Space Physics*, 1986, **91**(A5): 5557-5566

[41] DROB D P, EMMERT J T, CROWLEY G, *et al*. An empirical model of the Earth's horizontal wind fields: HWM07[J]. *Journal of Geophysical Research*: *Space Physics*, 2008, **113**(A12): A12304

[42] DROB D P, EMMERT J T, MERIWETHER J W, *et al*. An update to the Horizontal Wind Model (HWM): the quiet time thermosphere[J]. *Earth and Space Science*, 2015, **2**(7): 301-319

[43] DANG T, ZHANG B Z, LEI J H, *et al*. Azimuthal averaging–reconstruction filtering techniques for finite-difference general circulation models in spherical geometry[J]. *Geoscientific Model Development*, 2021, **14**(2): 859-873

[44] ROBLE R G, RIDLEY E C, RICHMOND A D, *et al*. A coupled thermosphere/ionosphere general circulation model[J]. *Geophysical Research Letters*, 1988, **15**(12): 1325-1328

[45] WEIMER D R. Improved ionospheric electrodynamic models and application to calculating Joule heating rates[J]. *Journal of Geophysical Research*: *Space Physics*, 2005, **110**(A5): A05306

Author Biography



ZHANG Ning female, was born in Tangshan, Hebei Province, in May 1992. She is currently a Senior Engineer at the Institute of Geology and Geophysics, Chinese Academy of Sciences. Her primary research interests include the detection techniques and data analysis of incoherent scatter radar (ISR) and the observation of ionospheric electric fields and neutral winds.
E-mail: zhangn@mail.iggcas.ac.cn



YUE Xin'an(**Corresponding author**) male, was born in Hubei Province in 1980. He is currently a Professor and Ph.D. Supervisor at the Institute of Geology and Geophysics, Chinese Academy of Sciences. His primary research interests include incoherent scatter radar (ISR) detection techniques, ionospheric physics, ionospheric numerical modeling and data assimilation, as well as related fundamental and applied fundamental research.
E-mail: yuexinan@mail.iggcas.ac.cn